Progress in Natural Science: Materials International 36 (2026) 168–174

HOSTED BY

Contents lists available at ScienceDirect

Progress in Natural Science: Materials International

journal homepage: www.elsevier.com/locate/pnsmi

Hollowing mechanism of noble metal nanoparticles during their Ag-templated synthesis

Zhong Zheng[a,b,1], Mengyuan Ma[b,c,1], Hui Liu[b], Dong Chen[b], Shaonan Tian[b,*], Xiwei Qi[a,**], Jun Yang[b,c,***]

[a] School of Resources and Materials, Northeastern University at Qinhuangdao, Qinhuangdao, 066004, China
[b] State Key Laboratory of Mesoscience and Engineering, Institute of Process Engineering, Chinese Academy of Sciences, Beijing, 100190, China
[c] Center of Materials Science and Optoelectronics Engineering, University of Chinese Academy of Sciences, Beijing, 100049, China

ARTICLE INFO

Keywords:
Noble metal nanostructures
Core@shell
Hollow
Kirkendall effect
Methanol oxidation reaction

ABSTRACT

Hollow noble metal nanostructures have broad applications in catalysis and other fields. Herein, we report that Ag@metal (Ag@M, M = Ru, Os, Ir, Pt, PtRu, PtRuOs) core@shell nanoparticles synthesized in oleylamine can transform into hollow AgM alloy nanoparticles via prolonged heating. The structural evolution mechanism is attributed to the Kirkendall effect, driven by unbalanced interdiffusion of Ag and M atoms: Ag atoms (with higher mobility) diffuse from the core to the shell more rapidly than M atoms, inducing vacancy flow and interface shift, ultimately forming hollow alloys with slightly reduced particle sizes. X-ray photoelectron spectroscopy reveals binding energy shifts of Ag and Pt in hollow AgPt alloys due to electronegativity differences. Electrochemical tests show that despite the lower electrochemically active surface area of hollow AgPt alloys caused by Ag-induced Pt dilution, their methanol oxidation reaction activity and onset potential are comparable to the core-shell precursors. This is because the ensemble effect from Ag-Pt alloying weakens CO adsorption on Pt sites, offsetting the dilution-induced negative effect. This study provides insights for designing efficient Ag-based nanoalloy electrocatalysts.

Given the important applications of hollow nanomaterials in fields such as catalysis [1–9], nanoreactor [10], sensing [11–13], battery [14,15], supercapacitor [16], and drug delivery [17,18], we have previously reported a universal strategy for preparing hollow monometallic and alloyed noble metal nanoparticles [19,20]. This method uses silver (Ag) nanoparticles as templates: core-shell structured nanoparticles are first fabricated with Ag as the core and monometal or alloy as the shell; these nanoparticles are then treated with either bis(p-sulfonatophenyl) phenylphosphane dihydrate dipotassium salt (BSPP) or saturated sodium chloride (NaCl) solution. The former has a strong complexing ability with Ag to form water-soluble complexes [19,21,22], while the latter first reacts with Ag to form silver chloride (AgCl) precipitates, which are then dissolved [20]. Both treatments can effectively remove the diffused Ag component, ultimately yielding hollow noble metal nanostructures.

However, in recent experiments, we found that after the preparation of Ag@M (where M represents a single noble metal or alloy) core@shell structured nanoparticles in oleylamine, simply extending the heating time can also induce the hollowing of the core-shell structure, ultimately yielding hollow nanoparticles. Of course, the shell layer of the hollow structure obtained in this way is not composed of a single noble metal or original alloy component, but an alloy formed by them and Ag. Therefore, in this study, based on the fundamental knowledge of materials science, we propose a reasonable structural evolution mechanism by tracking the transformation of Ag@M core-shell structures into hollow AgM alloy nanoparticles via transmission electron microscopy (TEM). Considering that in the widely used wet-chemistry methods, it is difficult to synthesize alloys of Ag with other noble metals even through the one-pot approach due to the differences in their redox potentials, this structural evolution is particularly significant for the preparation of Ag-

* Corresponding author.
** Corresponding author.
*** Corresponding author. State Key Laboratory of Mesoscience and Engineering, Institute of Process Engineering, Chinese Academy of Sciences, Beijing, 100190, China.
E-mail addresses: sntian@ipe.ac.cn (S. Tian), qixiwei@mail.neu.edu.cn (X. Qi), jyang@ipe.ac.cn (J. Yang).
[1] These authors made equal contributions to this study.

https://doi.org/10.1016/j.pnsc.2026.01.004
Received 24 December 2025; Received in revised form 4 January 2026; Accepted 8 January 2026
Available online 22 January 2026
1002-0071/© 2026 Chinese Materials Research Society. Published by Elsevier B.V. All rights are reserved, including those for text and data mining, AI training, and similar technologies.

based nanoalloys. Finally, we selected the hollow AgPt nanoparticles obtained after structural evolution as a typical sample and methanol electrocatalytic oxidation as a model reaction to investigate the effect of the Ag component in the hollow shell on the catalytic activity of noble metals, aiming to establish some experimental foundations for the design of high-efficiency electrocatalysts.

Oleylamine was employed as a capping agent and solvent as well as reducing agent to synthesize Ag nanoparticles, whose morphology, size, and crystallinity were characterized via TEM, size distribution analysis, and X-ray diffraction (XRD). Fig. S1a of Supplementary Material (SM) for the TEM image reveals well-dispersed, spherical nanoparticles with no observable aggregation, typical of oleylamine-stabilized metal nanoparticles [19,23]. The contrast (dark particles on a lighter background) is typical for metallic nanoparticles in TEM imaging, arising from electron scattering differences between the Ag particles and the supporting substrate. Quantitative size analysis (SM Fig. S1b) yields an average particle diameter of 7.4 nm with a standard deviation (σ) of 4.9 nm, indicating relatively narrow size uniformity (consistent with the appearance in TEM). The XRD pattern (SM Fig. S1c, 2θ range: 30–90°) confirms the crystalline structure of the Ag nanoparticles. The diffraction peaks are indexed to the face centered cubic (fcc) phase of metallic Ag (JCPDS 04–0783), with characteristic reflections at ca. 38°, 44°, 64°, 77°, and 81° for (111), (200), (220), (311), and (222) crystal planes, respectively, of which the strongest (111) peak is typical for fcc metals due to its highest atomic packing density. In addition, the peak widths (related to particle size via the Scherrer equation) align with the nanoscale dimensions measured in TEM.

Subsequently, the Ag nanoparticles were used as seeds to direct the synthesis of core@shell nanoparticles, which serves as the prerequisite step for observing structural evolution upon prolonged heating. Below, we take the Ag-Ru binary system as a typical example to elaborate on the characterization of its core@shell structure and the subsequent evolution process. Fig. 1a shows the TEM image of the core@shell Ag@Ru nanoparticles as-prepared in oleylamine, which exhibit quasi-spherical morphologies and have an average particle size of ca. 12.4 nm (SM Fig. S2a). Their core@shell construction could be validated by the energy-dispersive X-ray (EDX)-based Ag and Ru profiles of an arbitrarily selected single particle along the direction indicated by the white arrow under the high-angle annular dark-field scanning TEM (HAADF-STEM) mode. As suggested by Fig. 1b, the Ru signal presents throughout the particle whereas the Ag signal is only detected in the core region. Impressively, after further heating in oleylamine for 3 h at 320 °C, the core@shell Ag@Ru nanoparticles are evolved into AgRu alloy nanoparticles with hollow interiors, as evinced by the TEM image (Fig. 1c), in which an increase in the image contrast between the core and shell region is clearly observed. Fig. 1d shows EDX-based Ag and Ru profiles of an arbitrarily selected single particle after structural evolution, which suggest consistent distribution of Ag and Ru signals across the entire particle range, indicating a homogenization tendency of Ag and Ru during the evolution of Ag@Ru core@shell structures into hollow nanoparticles. Notably, after structural evolution, the as-obtained AgRu hollow alloy nanoparticles have an average particle size of 11.3 nm (SM Fig. S2b), which is slightly smaller than their core-shell predecessors before evolution.

Before explaining the evolution mechanism, we first sampled at different time and tracked the evolution process of Ag@Ru core@shell nanoparticles into hollow structures using TEM. The observations are shown in Fig. 2. After continuous heating for another 30 min, as shown in Fig. 2a for the TEM image, there are no significant differences in size, size distribution, or structure compared with the pre-formed Ag@Ru core@shell nanoparticles. However, when the heating time is further extended to 60 min, obvious changes in the particle structure can be

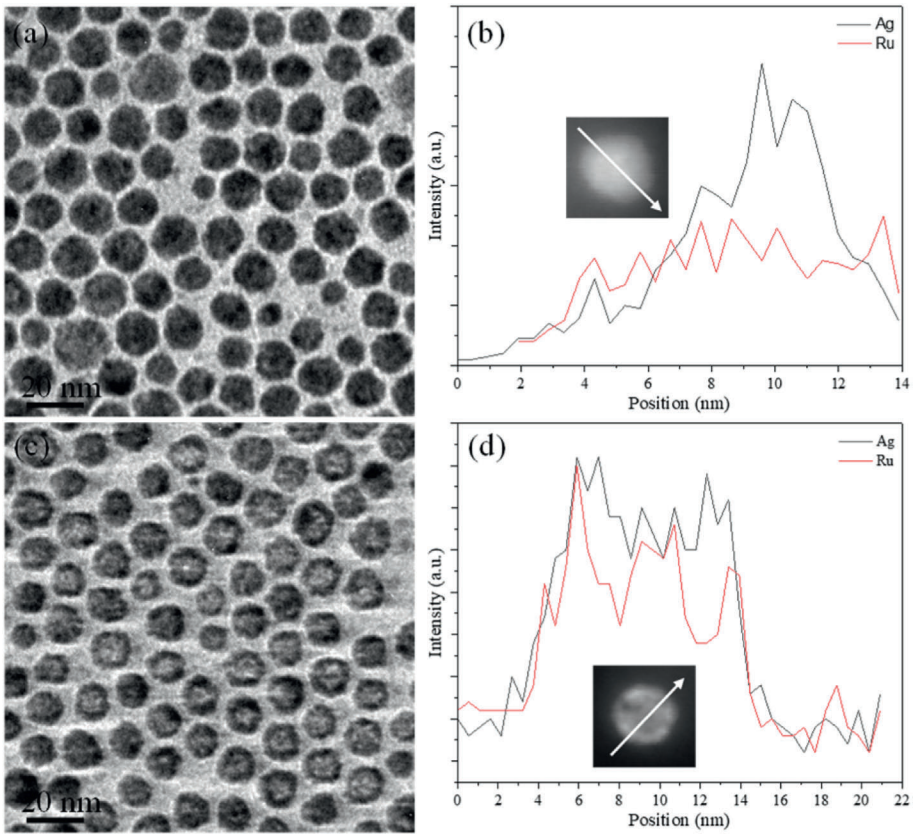

Fig. 1. (a,c) TEM images of the as-prepared core@shell Ag@Ru nanoparticles and (b,d) EDX-based Ag and Ru profiles of an arbitrarily selected core@shell Ag@Ru nanoparticle under STEM mode along the direction indicated by the white arrow before (a,b) and after structural evolution (c,d) in oleylamine at elevated temperature, respectively.

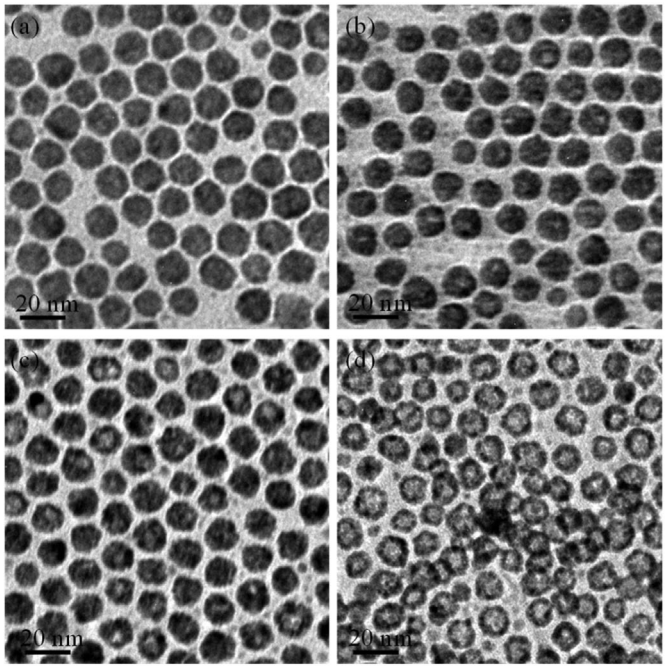

Fig. 2. Representative TEM images of the core@shell Ag@Ru nanoparticles after further heating in oleylamine for 30 min (a), 60 min (b), 90 min (c), and 120 min (d), respectively.

observed under TEM, with distinct cavities appearing in most particles, which exhibit significant contrast differences (Fig. 2b). After heating for 90 min, each particle exhibits further expanded cavities, as displayed by Fig. 2c for the TEM image. When the heating time reaches 120 min, as observed from the TEM image (Fig. 2d), each Ag@Ru core@shell particle evolves into a hollow-structured nanoparticle with an average size smaller than their core@shell precursors; no significant structural and size changes occur upon further heating thereafter, indicating that the structural evolution process has been completed.

Ultraviolet–visible (UV–vis) spectroscopy was also employed to monitor the structural evolution of Ag@Ru core@shell particles with prolonged heating time. As seen in SM Fig. S3, The Ag seeds exhibit a strong localized surface plasmon resonance (LSPR) peak cencered at ca. 408 nm, which is characteristic of Ag nanoparticles. For the as-prepared Ag@Ru core@shell particles (0.0 h), the LSPR peak intensity decreases and broadens compared to the Ag seeds, confirming the formation of the Ru shell (which quenches Ag's plasmon response). As continuous heating time increases (0.5 h–2.0 h), the residual Ag-related absorption (around 400 nm) continues to weaken and shift to longer wavelength, and the overall absorbance across the wavelength range gradually diminishes. This trend aligns with the structural transformation observed via TEM (hollow structure formation and size reduction): the progressive attenuation of the Ag LSPR signal reflects the dissolution/migration of Ag (the core) during heating, while the reduced absorbance corresponds to the smaller average size of the final hollow nanoparticles. By 2.0 h, the spectrum stabilizes, consistent with the TEM observation that structural evolution is complete, as no further changes in absorbance (or particle structure) occur with additional heating. Thus, the UV–Vis data provide complementary optical evidence for the time-dependent core@shell-to-hollow structural transition of Ag@Ru nanoparticles.

The hollowing process of Ag@Ru core@shell nanoparticles can be described using the schematic diagram shown in Fig. 3, and the underlying mechanism is the unbalanced interdiffusion between different metals, namely the Kirkendall effect [24–26], which can be elaborated through the following sequential processes. Firstly, the Ag@Ru core@shell structure itself constitutes a typical diffusion couple. Due to the mismatch in crystal structures and lattice constants between Ag and Ru, significant atomic distortion occurs at their interface; this distortion promotes the aggregation of crystal vacancies at the interface, and these accumulated vacancies further serve as effective channels for subsequent atomic diffusion. The core of this mechanism lies in the atomic diffusion discrepancy, which is the core manifestation of the Kirkendall effect. At the experimental temperature, Ag atoms (with a lower melting point) exhibit high mobility and thus diffuse rapidly in the Ru matrix, while Ru atoms (with a higher melting point) show much slower diffusion kinetics due to the experimental temperature being far below their melting point. This obvious difference in diffusion rates leads to an asymmetric atomic transport: the number of Ag atoms moving from the Ag core to the Ru shell is significantly greater than the number of Ru atoms diffusing in the opposite direction, ultimately forming a net flow of Ag atoms toward the Ru shell.

This net atomic flow is inevitably accompanied by a net flow of crystal vacancies in the reverse direction, i.e., vacancies move from the Ru shell to the Ag core, resulting in a distinct concentration imbalance of vacancies on both sides of the interface. Specifically, the continuous migration of vacancies to the Ag core causes the vacancy concentration on the Ru shell side to drop below the equilibrium value, while the Ag core side accumulates a large number of vacancies, making its vacancy concentration higher than the equilibrium value. When the system tends to thermodynamic stability, the vacancy concentrations on both sides gradually return to the equilibrium state. During this process, the Ru shell, which previously has a low vacancy concentration, elongates as it is replenished with vacancies, while the Ag core, which has an excessive vacancy concentration, shortens as vacancies are eliminated; this structural change directly drives the interface between Ag and Ru to shift a certain distance toward the Ag core side.

Eventually, this interface shift leads to the complete transformation of the original Ag@Ru core@shell structure into AgRu hollow alloy nanoparticles. Due to the contraction of the Ag core and the directional shift of the interface, the average particle size of the final hollow nanoparticles is slightly smaller than that of the original core@shell precursors, which is consistent with the structural characteristics observed in TEM images.

The hollowing phenomenon based on the mechanism illustrated in Fig. 3 is not exclusive to the Ag@Ru core@shell nanoparticles; similar phenomena have been observed in other core@shell systems with Ag as the core and other noble metals or alloys as the shell. Fig. 4a, e, i, m and q are the TEM images of the Ag@Os, Ag@Ir, Ag@Pt, Ag@PtRu and Ag@PtRuOs core@shell nanoparticles, which were synthesized by a slightly modified method reported in the literature (see SM for experimental details) [19]. In contrast, Fig. 4c, g, k, o and s are the TEM images of the samples after further heating at the corresponding synthesis temperature for 2 h. Obviously, the heat-treated particles exhibit distinct hollow structures, and the contrast difference between the core and the shell regions in their TEM images is more pronounced compared with that of their core@shell precursors. Also, Similar to the Ag@Ru core@shell particles, as illustrated by the particle size distribution histograms in Fig. 4, after Ag@Os, Ag@Ir, Ag@Pt, Ag@PtRu, and Ag@PtRuOs core@shell nanoparticles are further heated and transformed into their corresponding hollow alloy nanoparticles, their average particle sizes all decrease to a certain extent. This is also attributed to the shift of the core@shell interface toward the side of the metal with a faster diffusion rate.

To investigate the effect of Ag residing in the core and diffusing into the shell on the electrocatalytic performance of active metals, we selected Ag@Pt core@shell nanoparticles and corresponding AgPt hollow nanoalloys after hollowing process as representative samples to evaluate and compare their activity and stability toward the methanol oxidation reaction (MOR). Prior to the electrocatalytic tests, we first analyzed the chemical states of each metal in the Ag@Pt core@shell nanoparticles and AgPt hollow alloy nanoparticles. As shown by Fig. 5a−d, before and after the structural evolution of Ag@Pt core@shell nanoparticles, the X-ray photoelectron spectroscopy (XPS) spectra of Ag

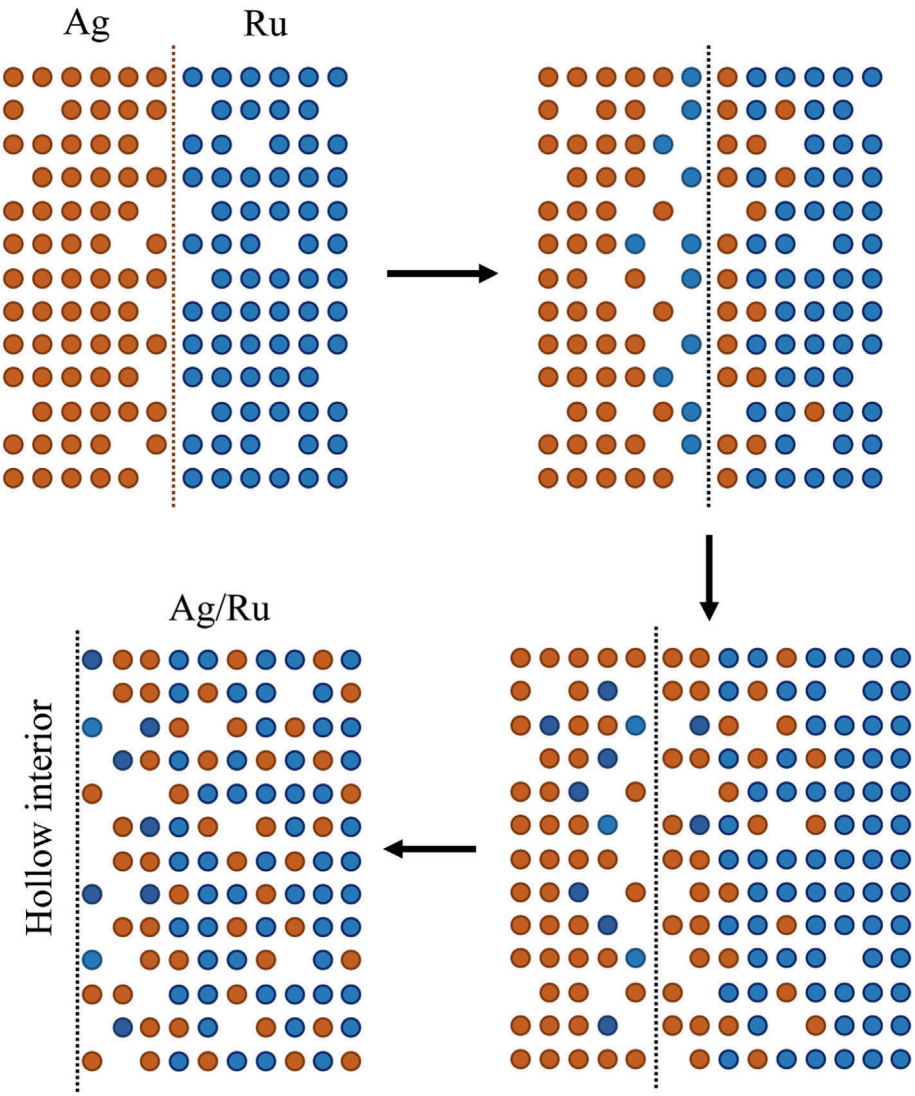

Fig. 3. Schematic illustration showing the hollowing mechanism of core@shell Ag@Ru nanoparticles via unbalanced interdiffusion between different metals (Kirkendall effect) at elevated temperature.

in the samples both exhibit a pair of peaks corresponding to metallic Ag (0) (368.0 eV of $3d_{5/2}$ and 374.0 eV of $3d_{3/2}$ for Ag in Ag@Pt core@shell nanoparticles; 368.4 eV of $3d_{5/2}$ and 374.4 eV of $3d_{3/2}$ for Ag in AgPt hollow alloy nanoparticles) [27]. In contrast, the XPS spectra of Pt display two pairs of peaks: the pair with lower binding energy (69.9 eV of $4f_{7/2}$ and 73.3 eV of $4f_{5/2}$ for Pt in Ag@Pt core@shell nanoparticles; 69.5 eV of $4f_{7/2}$ and 72.9 eV of $4f_{5/2}$ for Pt in AgPt hollow alloy nanoparticles) and higher signal intensity is attributed to metallic Pt(0), while the pair with higher binding energy (71.4 eV of $4f_{7/2}$ and 74.7 eV of $4f_{5/2}$ for Pt in Ag@Pt core@shell nanoparticles; 70.9 eV of $4f_{7/2}$ and 74.3 eV of $4f_{5/2}$ for Pt in AgPt hollow alloy nanoparticles) and lower signal intensity corresponds to oxidized Pt species (e.g., PtO) [28–30]. However, as summarized in SM Table S1, compared with their core-shell precursors (Fig. 5a and b), the binding energies of both Ag and Pt in the hollow AgPt alloy nanoparticles formed after structural evolution exhibit a shift (Fig. 5c and d): the former increases to a certain extent, while the latter decreases slightly. This phenomenon may be related to the electronegativity of Ag and Pt, which are 1.9 and 2.2, respectively. In the homogeneous AgPt alloy, the influence of this electronegativity difference on the XPS binding energies of the elements is more pronounced than that in the core-shell structure, resulting in the observable binding energy shifts in the XPS spectra.

The core@shell Ag@Pt nanoparticles before and after structural evolution were loaded on the Vulcan carbon substrate for estimating their electrocatalytic activities for MOR at room-temperature. As exhibited by SM Fig. S4 for the representative TEM images, both the core@shell Ag@Pt nanoparticles and the hollow AgPt alloy nanoparticles as-prepared from structural evolution were evenly distributed on the carbon substrate, with mass loading fixed at 20 wt% for total Ag and Pt.

The electrochemically active surface areas (ECSAs) of core@shell Ag@Pt nanoparticles before and after structural evolution were determined using cyclic voltammetry. As shown in Fig. 5e, the ECSAs calculated by integrating the charge associated with the hydrogen adsorption/desorption potential region after double-layer correction, are 36.4 $m^2\ g_{Pt}^{-1}$ for core@shell Ag@Pt, and 20.5 $m^2\ g_{Pt}^{-1}$ for the hollow AgPt alloy nanoparticles as-synthesized from structural evolution, respectively. The relatively low ECSAs of the hollow AgPt alloy nanoparticles are probably attributed to the dilution effect of Pt atoms induced by alloying with Ag atoms, and their inner surfaces are also difficult to serve as effective active sites for the electrochemical reactions.

The MOR voltammograms over core@shell Ag@Pt and hollow AgPt alloy nanoparticles were shown in Fig. 5f. The peak current densities of hollow AgPt alloy nanoparticles normalized by the total mass loaded on the electrode for the forward and backward scans are 0.89 A mg^{-1} and

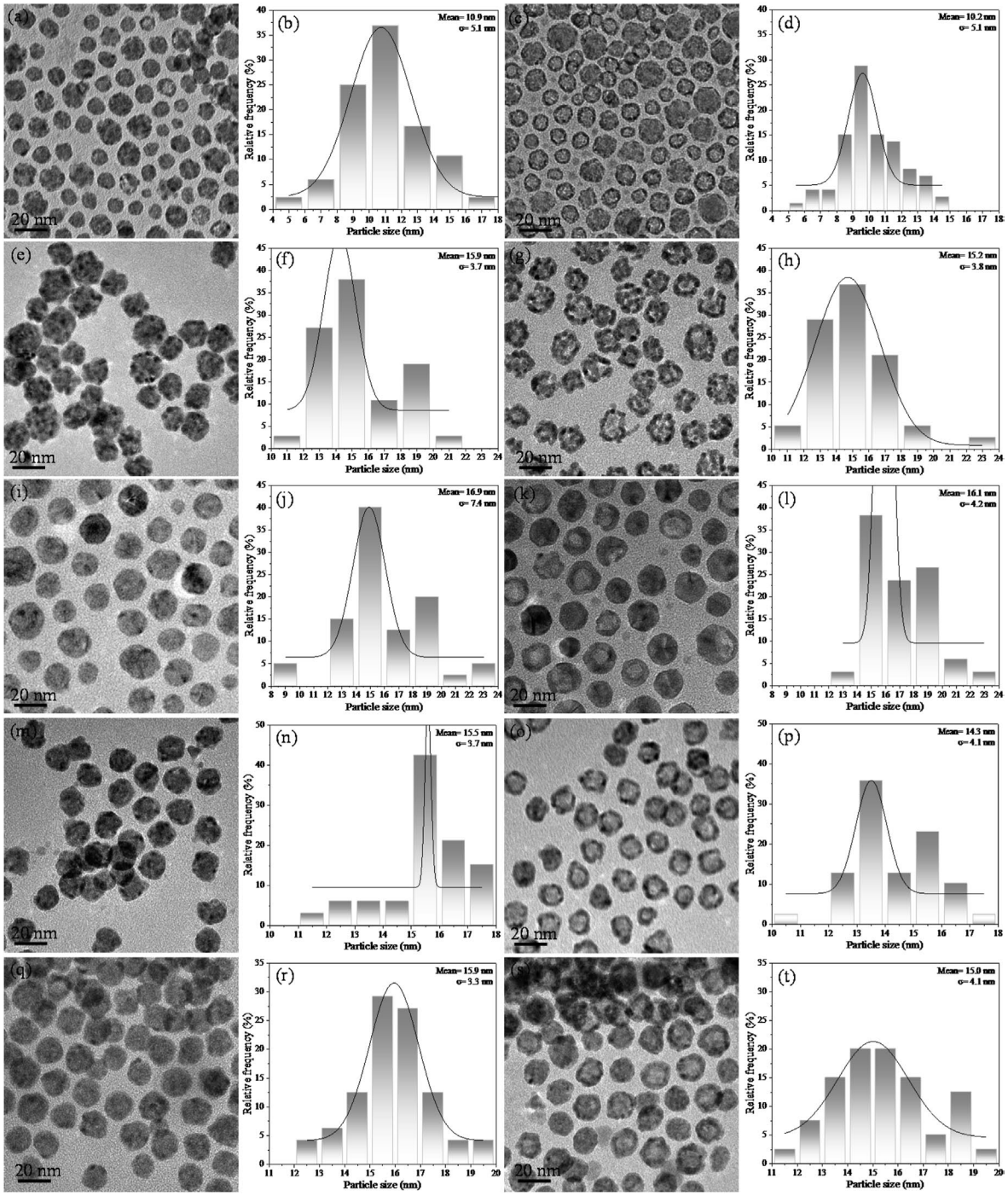

Fig. 4. (a,c,e,g,i,k,m,o,q,s)TEM images and (b,d,f,h,j,l,n,p,r,t) corresponding particle size histograms of the as-prepared core@shell Ag@Os (a–d), Ag@Ir (e–h), Ag@Pt (i–l), Ag@PtRu (m–p), and Ag@PtRuOs nanoparticles (q–t) before (a,b,e,f,i,j,m,n,q,r) and after structural evolution (c,d,g,h,k,l,o,p,s,t) in oleylamine at elevated temperature, respectively.

1.42 A mg^{-1}, respectively, which are almost identical to those of their core@shell Ag@Pt precursors (0.79 A mg^{-1} and 1.23 A mg^{-1}, respectively). In addition, as observed from Fig. 5f, these two samples also exhibit almost no difference in the onset potential (crosspoint between the *x* axis and the linear segment of the CV curves) for MOR. Theoretically, after the Ag@Pt core-shell nanoparticles evolve into hollow AgPt alloy nanoparticles upon prolonged heating, the dilution effect of Ag atoms on the Pt surface should render the hollow AgPt nanoparticles less active than the corresponding Ag@Pt core-shell counterparts in the MOR. However, the alloying of Ag with Pt gives rise to an ensemble effect, which is defined as the influence of heteroatom doping in the vicinity of active sites and is closely correlated with the composition of heteroatoms [31]. Through density functional theory (DFT) calculations, Liu and Nørskov have demonstrated that the ensemble effect can be well-described by a simple linear interpolation model, wherein the adsorption energy of small molecules at an ensemble site approximates the average of its constituent components [32]. Considering that CO is not only an intermediate product of the MOR but also the primary species causing poisoning of Pt-based catalysts, and Ag is a well-documented metal with weak CO adsorption capability owing to its low d-band center [33–35], alloying with Ag can thus effectively weaken the adsorption strength of CO on Pt active sites and thereby enhance the

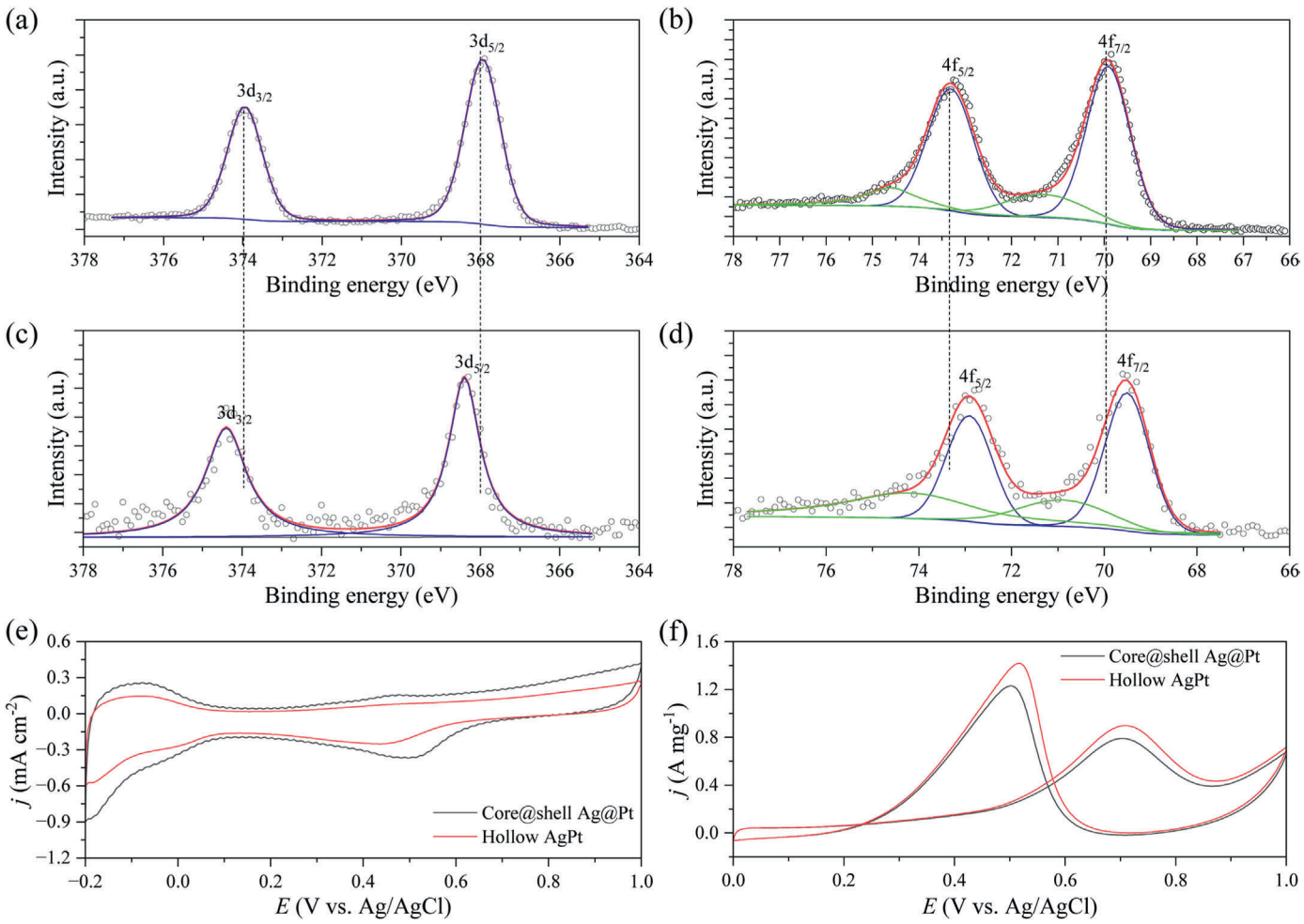

Fig. 5. (a,c) 3d XPS spectra of Ag and (b,d) 4f XPS spectra of Pt in core@shell Ag@Pt (a,b), and hollow AgPt alloy nanoparticles (c,d); (e) cyclic voltammograms of core@shell Ag@Pt, and hollow AgPt alloy nanoparticles in argon-purged $HClO_4$ electrolyte (0.1 M) at a scan rate of 50 mV s^{-1}; (f) cyclic voltammograms of core@shell Ag@Pt, and hollow AgPt alloy nanoparticles in argon-purged $HClO_4$ (0.1 M) with methanol (1 M) at a scan rate of 20 mV s^{-1}.

catalytic activity for MOR. This positive effect counteracts the negative effect arising from the dilution of active surfaces, resulting in nearly unchanged MOR activity of the alloy nanoparticles formed after hollowing process.

In summary, in this study, we systematically investigated the structural evolution of Ag@M (M = Ru, Os, Ir, Pt, PtRu, PtRuOs) core@shell nanoparticles synthesized in oleylamine upon prolonged heating. A universal hollowing phenomenon was observed, with core@shell structures transforming into hollow AgM alloy nanoparticles, which is attributed to the Kirkendall effect induced by unbalanced interdiffusion of Ag and M atoms. Ag atoms with higher mobility diffuse from the core to the shell more rapidly than M atoms, triggering vacancy flow and interface shift toward the Ag core, ultimately resulting in hollow alloys with slightly reduced particle sizes. XPS analysis reveals that Ag and Pt in hollow AgPt alloys exhibit binding energy shifts compared to their core-shell precursors, which is associated with the more pronounced electronegativity difference effect in homogeneous alloys. Electrochemical tests demonstrate that despite the lower electrochemically active surface area of hollow AgPt alloys caused by Ag-induced Pt dilution, their MOR activity and onset potential are comparable to the core-shell counterparts. This balance stems from the ensemble effect of Ag-Pt alloying, which weakens CO adsorption on Pt active sites and offsets the dilution-induced negative effect. This work not only provides a deep understanding of the heat-driven Kirkendall effect in Ag-templated noble metal nanostructures but also offers a facile strategy for synthesizing Ag-based nanoalloys that are challenging to prepare via conventional wet-chemistry methods. The insights gained herein lay experimental foundations for the rational design of high-performance noble metal electrocatalysts for energy conversion applications.

CRediT authorship contribution statement

Zhong Zheng: Validation, Methodology, Investigation, Data curation. **Mengyuan Ma:** Investigation, Formal analysis, Data curation. **Hui Liu:** Validation, Data curation. **Dong Chen:** Investigation, Formal analysis. **Shaonan Tian:** Writing – review & editing, Validation, Supervision, Resources, Investigation, Funding acquisition. **Xiwei Qi:** Writing – review & editing, Validation, Supervision, Resources. **Jun Yang:** Writing – review & editing, Writing – original draft, Supervision, Project administration, Investigation, Funding acquisition, Conceptualization.

Declaration of competing interest

We declare that there are no conflicts of interest in relation to the manuscript. We confirm that the results and interpretations reported in the manuscript are original and have not been plagiarized. We also certify that we have disclosed any financial or non-financial relationships that may be interpreted as constituting a conflict of interest in relation to this manuscript.

Acknowledgments

We gratefully acknowledge the financial supports from the Full-Time High-Level Talent Introduction Support Fund for Jun Yang (2023HBQZYCXY031), Energy Revolution S&T Program of Yulin Innovation Institute of Clean Energy (E411060705), the National Natural Science Foundation of China (22272179, 42307326), CAS Project for Young Scientists in Basic Research (YSBR-044), and State Key Laboratory of Mesoscience and Engineering, Institute of Process Engineering, Chinese Academy of Sciences (MESO-24-A01).

Appendix A. Supplementary data

Supplementary data to this article can be found online at https://doi.org/10.1016/j.pnsc.2026.01.004.

References

[1] J.W. Hong, S.W. Kang, B.-S. Choi, D. Kim, S.B. Lee, S.W. Han, Controlled synthesis of Pd–Pt alloy hollow nanostructures with enhanced catalytic activities for oxygen reduction, ACS Nano 6 (2012) 2410–2419.
[2] G. Prieto, H. Tüysüz, N. Duyckaerts, J. Knossalla, G.-H. Wang, F. Schüth, Hollow and microstructures as catalysts, Chem. Rev. 116 (2016) 14056–14119.
[3] L. Yu, H.B. Wu, X.W.D. Lou, Self-templated formation of hollow structures for electrochemical energy applications, Acc. Chem. Res. 50 (2017) 293–301.
[4] G. Zhu, J. Liu, S. Li, Y. Zuo, D. Li, H. Han, Nickel-ion-oriented fabrication of spiny PtCu alloy octahedral nanoframes with enhanced electrocatalytic performance, ACS Appl. Energy Mater. 2 (2019) 2862–2869.
[5] W. Zhang, X. Guo, C. Li, J.-Y. Xue, W.-Y. Xu, Z. Niu, H. Gu, C. Redshaw, J.-P. Lang, Ultralong nitrogen/sulfur Co-doped carbon nano-hollow-sphere chains with encapsulated cobalt nanoparticles for highly efficient oxygen electrocatalysis, Carbon Energy 5 (2023) e317.
[6] J. Pan, X. Yang, J. Zhou, W. Cheng, K. Cheng, Novel ZIF-8/ZnS hollow polyhedral heterostructures derived from ZIF-8 with enhanced photocatalytic activity for degradation of aflatoxin B_1, Prog. Nat. Sci. Mater. Int. 33 (2023) 575–580.
[7] S.E. Son, P.K. Gupta, W. Hur, H.B. Lee, D.K. Han, G.H. Seong, Hollow ruthenium nanoparticles with enhanced catalytic activity for colorimetric detection of C-reactive protein, ACS Appl. Nano Mater. 6 (2023) 11435–11442.
[8] Y. Wu, M. Song, Z. Zhao, G.-H. Wang, C. Wang, D. Astruc, Integrating theory with the nanoreactor concept to synthesize hollow carbon sphere-encapsulated PtNi alloys for enhanced H_2 generation, Carbon Energy 6 (2024) e455.
[9] S. Feng, S. Fan, L. Li, Z. Sun, H. Tang, Y. Xu, L. Fang, C. Wang, Using hollow dodecahedral NiCo-LDH with multi-active sites to modify $BiVO_4$ photoanode facilitates the photoelectrochemical water splitting performance, Nano Res. Energy 3 (2024) e9120117.
[10] S. Zhu, Q. Zhao, H. Guo, L. Liu, X. Wang, X. Qi, X. Meng, W. Cui, Construction of a Cu@hollow TS-1 nanoreactor based on a hierarchical full-spectrum solar light utilization strategy for photothermal synergistic artificial photosynthesis, Carbon Energy 6 (2024) e499.
[11] H. Hu, H. Liang, J. Fan, L. Guo, H. Li, N.F. de Rooij, A. Umar, H. Algami, Y. Wang, G. Zhou, Assembling hollow cactus-like ZnO nanorods with dipole-modified graphene nanosheets for practical room-temperature formaldehyde sensing, ACS Appl. Mater. Interfaces 14 (2022) 13186–13195.
[12] D. Mandal, S. Priya, A. Chowdhury, A.K. Srivastava, A. Chandra, Hollow nanostructures of ternary $Ce_{1-x}Cu_xO_2$ for volatile organic compound sensing, ACS Appl. Nano Mater. 7 (2024) 476–486.
[13] L. Chen, C.-C. Liu, T.-Y. Yang, Y.-X. Liu, Y.-Q. Zhang, Z. Guo, Porous SnO_2 nanofibers embedded with hollow hetero-metal oxide nanospheres for enhanced gas sensing, ACS Appl. Mater. Interfaces 17 (2025) 55097–55106.
[14] J. Xu, H. Zhang, R. Wang, P. Xu, Y. Tong, Q. Lu, F. Gao, Delicate control of multishelled zn–mn–o hollow microspheres as a high-performance anode for lithium-ion batteries, Langmuir 34 (2018) 1242–1248.
[15] X.-S. Tao, X. Li, E.-W. Hou, Z. Ma, K. Yang, J. Ma, J. Sha, Construction of uniform CuO nanoshells and its application in high-voltage cathode materials, Prog. Nat. Sci. Mater. Int. 34 (2024) 747–752.
[16] M.M. Vadiyar, J.-Y. Kim, J.-H. Bae, K.-W. Nam, Imidazole linker-induced covalent triazine framework–ZIF hybrids for confined hollow carbon super-heterostructures toward a long-life supercapacitor, Carbon Energy 5 (2023) e344.
[17] J. Chen, X. Wu, X. Hou, X. Su, Q. Chu, N. Fahruddin, J.X. Zhao, Shape-tunable hollow silica nanomaterials based on a soft-templating method and their application as a drug carrier, ACS Appl. Mater. Interfaces 6 (2014) 21921–21930.
[18] B. Yang, W. Qian, L. Zhang, Processing solid hydrogels into hollow structures by infrared laser light for highly-efficient drug loading and controlled release, Langmuir 40 (2024) 22736–22743.
[19] H. Liu, J. Qu, Y. Chen, J. Li, F. Ye, J.Y. Lee, J. Yang, Hollow and cage-bell structured nanomaterials of noble metals, J. Am. Chem. Soc. 134 (2012) 11602–11610.
[20] H. Liu, F. Ye, J. Yang, A universal and cost-effective approach to the synthesis of carbon-supported noble metal nanoparticles with hollow interiors, Ind. Eng. Chem. Res. 53 (2014) 5925–5931.
[21] J. Yang, J.Y. Lee, H.-P. Too, S. Valiyaveettil, A bis(p-sulfonatophenyl) phenylphosphine-based synthesis of hollow Pt nanospheres, J. Phys. Chem. B 110 (2006) 125–129.
[22] Y.-N. Tan, J. Yang, J.Y. Lee, I.C.D. Wang, Mechanistic study on the bis(p-sulfonatophenyl)phenylphosphine synthesis of monometallic Pt hollow nanoboxes using Ag-Pt core-shell nanocubes as sacrificial templates, J. Phys. Chem. C 111 (2007) 14084–14090.
[23] D. Liu, Y. Zhang, H. Liu, P. Rao, L. Xu, D. Chen, X. Tian, J. Yang, Acetic acid-assisted mild dealloying of fine CuPd nanoalloys achieving compressive strain towards high-efficiency oxygen reduction and ethanol oxidation electrocatalysis, Carbon Energy 5 (2023) e324.
[24] Y. Yin, R.M. Rioux, C.K. Erdonmez, S. Hughes, G.A. Somorjai, A.P. Alivisatos, Formation of hollow nanocrystals through the nanoscale Kirkendall effect, Science 304 (2004) 711–714.
[25] M. Pang, J. Hu, H.C. Zeng, Synthesis, morphological control, and antibacterial properties of hollow/solid Ag_2S/Ag heterodimers, J. Am. Chem. Soc. 132 (2010) 10771–10785.
[26] L. Han, H. Liu, P. Cui, Z. Peng, S. Zhang, J. Yang, Alloy Cu_3Pt nanoframes through the structure evolution in Cu-Pt nanoparticles with a core-shell construction, Sci. Rep. 4 (2014) 6414.
[27] J. Yang, J.Y. Lee, H.-P. Too, A general phase transfer protocol for synthesizing alkylamine-stabilized nanoparticles of noble metals, Anal. Chim. Acta 588 (2007) 34–41.
[28] Q. Zeng, S. Tian, Y. Zhang, H. Liu, D. Chen, X. Tian, C. Hu, J. Yang, Phase transfer-based high-efficiency recycling of precious metal electrocatalysts, Green Chem. Eng. 5 (2024) 68–74.
[29] L. Chu, Z. Rong, M. Ma, F. Guo, S. Tian, J. Yang, Dodecylamine-mediated synthesis of caron-supported platinum-ruthenium alloy nanoparticles with ultrafine sizes towards high-efficiency methanol oxidation electrocatalysis, Prog. Nat. Sci. Mater. Int. 35 (2025) 215–221.
[30] Q. Zeng, M. Ma, H. Liu, L. Xu, S. Tian, D. Chen, J. Wang, J. Yang, Gold-catalyzed construction of atomically rough surfaces towards high-efficiency ethanol electrooxidation, Sci. Bull. 70 (2025) 2604–2615.
[31] J.W.A. Sachtler, G.A. Somorjai, Influence of ensemble size on CO chemisorption and catalytic *n*-hexane conversion by Au-Pt(111) bimetallic single-crystal surfaces, J. Catal. 81 (1983) 77–94.
[32] P. Liu, J.K. Nørskov, Ligand and ensemble effects in adsorption on alloy surfaces, Phys. Chem. Chem. Phys. 3 (2001) 3814–3818.
[33] B. Hammer, Y. Morikawa, J.K. Nørskov, CO chemisorption at metal surfaces and overlayers, Phys. Rev. Lett. 76 (1996) 2141–2144.
[34] A. Ruban, B. Hammer, P. Stoltze, H.L. Skriver, J.K. Nørskov, Surface electronic structure and reactivity of transition and noble metals, J. Mol. Catal. A: Chem. 115 (1997) 421–429.
[35] B. Hammer, J.K. Nørskov, Theoretical surface science and catalysis – calculations and concepts, Adv. Catal. 45 (2000) 71–129.